Philosophical Magazine,
Vol. 86, No. 36, 21 December 2006, 5847–5866

Taylor & Francis
Taylor & Francis Group

An experimentally-based viscoelastic constitutive model for polyurea, including pressure and temperature effects

A. V. AMIRKHIZI, J. ISAACS,
J. McGEE and S. NEMAT-NASSER*

Mechanical and Aerospace Engineering, Center of Excellence for Advanced Materials, University of California, San Diego, CA, USA

(*Received 24 October 2005; in final form 21 May 2006*)

Presented here are the results of a systematic study of the viscoelastic properties of polyurea over broad ranges of strain rates and temperatures, including the high-pressure effects on the material response. Based on a set of experiments and a master curve developed by Knauss (W.G. Knauss, *Viscoelastic Material Characterization relative to Constitutive and Failure Response of an Elastomer*, Interim Report to the Office of Naval Research (GALCIT, Pasadena, CA, 2003.) for time–temperature equivalence, we have produced a model for the large deformation viscoelastic response of this elastomer. Higher strain-rate data are obtained using Hopkinson bar experiments. The data suggest that the response of this class of polymers is strongly pressure dependent. We show that the inclusion of linear pressure sensitivity successfully reproduces the results of the Hopkinson bar experiments. In addition, we also present an equivalent but approximate model that involves only a finite number of internal state variables and is specifically tailored for implementation into explicit finite-element codes. The model incorporates the classical Williams–Landel–Ferry (WLF) time–temperature transformation and pressure sensitivity (M.L. Williams, R.F. Landel, and J.D. Ferry, *J. Am. Chem. Soc.*, **77** 3701 (1955)), in addition to a thermodynamically sound dissipation mechanism. Finally, we show that using this model for the shear behaviour of polyurea along with the elastic bulk response, one can successfully reproduce the very high strain rate pressure–shear experimental results recently reported by Jiao *et al.* (T. Jiao, R.J. Clifton and S.E. Grunschel, *Shock Compression of Condensed Matter 2005* (American Institute of Physics, New York, 2005.).

1. Introduction

Polyurea and polyurethane are general names for a wide range of polymeric materials that have been used extensively in the coating industry in solid elastomeric or rigid form. Here, we focus mainly on the properties and applications of polyurea in its solid elastomeric form. From truck bed abrasion protection to concrete elements surface enhancement, the material shows excellent characteristics, including, but not limited to, environmental and safety compliance, long-term stability, appearance and high mechanical performance [4]. Introduced in 1989 by Texaco

*Corresponding author. Email: sia@ucsd.edu

Philosophical Magazine
ISSN 1478–6435 print/ISSN 1478–6443 online © 2006 Taylor & Francis
http://www.tandf.co.uk/journals
DOI: 10.1080/14786430600833198

Chemical Company, polyurea was regarded as a product that did not fulfil the exaggerated expectations initially advertised, especially in the coating industry. As a result, many of its true benefits and advantages were not fully appreciated. Recent studies, however, have shown promising mechanical responses for polyurea that are not limited to only the coating applications but venture into critical applications such as reinforcement of metal structures against blast and impact loads.

Initially, manufacturers did not clearly differentiate between polyurethane and polyurea, identifying both classes of polymers as "polyurethanes". More recently, however, companies began to distinguish these products. Polyurethane was first developed by Otto Bayer and coworkers in the late 1930s and early 1940s [5]. The main components are di- or polyisocyanate molecules (cyanate functional group –NCO) exothermically reacting with polyols (hydroxyl functional group –OH) and forming extended chains and networks bonded by urethane groups, –O(CO)(NH)–. In polyurea, polyols are switched with amine molecules (functional group $–NH_2$) resulting in polymers with urea bonding, –(NH)(CO)(NH)–. This generally involves faster reaction times than those associated with polyurethane. In fact, the fast reaction time makes it possible to apply polyurea as spray in coating applications.

The physical properties of polyurea vary with the composition. The service temperature typically ranges between -50 to 150°C. The elongation at tearing can be as high as 800%. The specific material discussed in the present paper is based on Isonate® 2143L [6] and Versalink® P1000 [7]. A five percent excess of Isonate® 2143L is used to produce a lightly cross-linked polymer [8]. The glass transition temperature, T_g, is below -50°C [1, 8]. In addition, polyurea exhibits a very stiff nearly-elastic response to volumetric deformations, whereas (above T_g) its shearing response at moderate pressures and strain rates is soft and viscoelastic, so that its laterally unconfined axial deformation is nearly incompressible.

Recent studies show that applying a layer of polyurea backing to steel plates significantly enhances the resistance of the composite structure to impact and blast loading. Various tests show that this improvement can change the response from full penetration of a projectile to fully eliminating fracturing [9]. The real mechanism underlying this effect is not yet fully understood and formulated. The objective of the present paper and related research on modelling and impact testing of and fracturing such composites is to understand and illuminate this underlying mechanism and develop physics-based constitutive models for the high strain rate response of the elastomer. In doing so, we have learned that the linear viscoelasticity with the Williams–Landel–Ferry time–temperature transformation and linear pressure sensitivity seem to account for the material response with reasonable accuracy [2]. Here, we show that this model successfully reproduces many of the observed high strain-rate test results for polyurea.

2. Time–temperature superposition

To formulate the temperature- and pressure-dependent response of polymers such as polyurea, tentatively consider the possibility of using linear viscoelasticity [10]

and then seek to modify this if necessary. For small strains, linear viscoelasticity defines the stress at time t in terms of the history of the strain rate by

$$\boldsymbol{\sigma}(t) = \int_{-\infty}^{t} \boldsymbol{\chi}(t-\tau) : \dot{\boldsymbol{\varepsilon}}(\tau) d\tau. \tag{1}$$

Here $\dot{\boldsymbol{\varepsilon}}$ is the (small strain) strain-rate tensor, $\boldsymbol{\sigma}$ is the Cauchy stress tensor and $\boldsymbol{\chi}$ is the fourth-order relaxation modulus tensor. This relation may be generalized to finite strains and small rotations using

$$\boldsymbol{\sigma}(t) = \int_{-\infty}^{t} \boldsymbol{\chi}(t-\tau) : \mathbf{D}(\tau) d\tau, \tag{2}$$

where $\mathbf{D}$ is the deformation-rate tensor, i.e. the symmetric part of the velocity gradient. To ensure objectivity for large rotations, this equation will have to be properly modified. The necessary modification is only geometrical and can be implemented in various ways [11, 12]. In the present work, we focus on the material description, and this is not affected by such required geometric transformations. We also assume that $\boldsymbol{\chi}(t)$ does not have a singularity at $t=0$ The inclusion of a delta function singularity at $t=0$ eliminates the possibility of an instantaneous deformation under finite force. Although this may be physically appropriate, it is ignored for linearly elastic materials. We simplify our discussion of viscoelasticity by including the assumption of instantaneous elasticity, i.e., regularity of the relaxation moduli at $t=0$.

We limit attention to the isotropic case, and set

$$\boldsymbol{\chi}(t) = 3K(t)\mathbf{E}^1 + 2G(t)\mathbf{E}^2, \tag{3}$$

where K and G are, respectively, the bulk and shear moduli and the fourth-order tensors $\mathbf{E}^1$ and $\mathbf{E}^2$ have the following rectangular Cartesian components:

$$E^1_{ijkl} = \delta_{ij}\delta_{kl}/3, \tag{4}$$

$$E^2_{ijkl} = 1^{(4s)}_{ijkl} - E^1_{ijkl} = \left(\delta_{ik}\delta_{jl} + \delta_{il}\delta_{jk}\right)/2 - \delta_{ij}\delta_{kl}/3, \tag{5}$$

where δ_{ij} is the Kronecker delta. This representation separates the deviatoric and the dilatational components of the deformation, and is suitable for our analysis, since the deviatoric response of most polymers is significantly different from their dilatational response. At ordinary pressures, the bulk modulus of this class of materials is usually orders of magnitude larger than their shear modulus. Furthermore, in most cases, the dilatational response of polymers, including that of polyurea, can be effectively modelled as elastic, since the dissipative mechanisms that are activated in dilatational deformations of most polymers are usually different, especially in their time scales, from the ones that are activated during their volume-preserving deformations.

Due to its high bulk modulus, measurement of the relaxation modulus of polyurea in uniaxial stress tests effectively produces its shear relaxation modulus. To see this, note that the Young modulus of an isotropic linearly elastic material is given by

$$E = \frac{9KG}{3K+G}. \tag{6}$$

When $G \ll K$ this simplifies to $E \approx 3G$. For isotropic viscoelastic materials, one can also argue that a high bulk modulus effectively keeps the volume preserved in a uniaxial stress test. Therefore, the instantaneous Poisson's ratio, defined as the ratio of the transverse to the longitudinal strain at instant t, is very close to 0.5, which means that

$$G(t) = \frac{E(t)}{2(1 + \nu_{\text{inst.}})}. \tag{7}$$

In the present paper, we use $\nu_{\text{inst.}} = 0.486$ and $\nu_{\text{inst.}} = 0.484$ for polyurea. The former value has been obtained using confined Hopkinson-bar tests that allow for the measurement of the transverse strain along with the corresponding axial strain and stress (for details, see Amirkhizi *et al.* [13]). The latter value is reported by Clifton and Jiao [14].

The linear elastic response for the bulk deformation usually yields stress–strain curves that are concave down. In other words, the tangential stiffness decreases with increasing deformation. This in not what we have observed in our tests of polyurea. Therefore, for modelling of the Hopkinson bar tests we use a physically-based model proposed by Anand [15]. This model is an isotropic thermodynamics-based constitutive representation appropriate for compressible elastomeric solids; it generalizes the well-known Arruda–Boyce model [16]. For bulk deformations, the model assumes

$$tr(\sigma) = 3\kappa \frac{\ln J}{J}, \tag{8}$$

where κ is a modified bulk modulus that depends linearly on the temperature, and J is the Jacobian of the deformation, respectively given by

$$\kappa(T) = \kappa(T_{ref}) + m(T - T_{ref}), \tag{9}$$

$$J = \det \mathbf{F}. \tag{10}$$

Equations (1)–(5) pertain to the isothermal deformations. For polymers, the temperature modifies the response in two ways, as discussed by Pipkin [17]. Firstly, the long-time moduli change essentially in proportion to the absolute temperature,

$$\lim_{t \to \infty} \frac{G(t,T)}{G(t,T')} = \frac{T}{T'}. \tag{11}$$

Secondly, due to the higher thermal energy at higher temperatures, the molecular relaxation processes are more easily and frequently activated. This translates into a shift to a smaller time parameter. Williams *et al.* [2] implemented these two effects empirically using the following expression:

$$G(t,T) = \frac{T}{T_{ref}} G_{ref}\left(\frac{t}{a(T)}\right). \tag{12}$$

Here G_{ref} is the relaxation modulus measured at the reference temperature, T_{ref}, and $a(T)$ is the time-temperature shift function that depends on the current temperature and the glass transition temperature, T_g, of the material. The range of the

applicability of this formula is usually limited to that between the glass transition temperature, T_g, and $T_g + 100\,\mathrm{K}$. Williams *et al.* [2] give an empirical expression for $a(T)$ that has only one material parameter, T_g, namely

$$\ln a(T) = -\frac{17.44(T - T_g)}{51.6 + T - T_g}. \tag{13}$$

Recently, Rahouadj *et al.* [18] have used a theoretical approach to arrive at this result starting from a thermodynamic framework of relaxation processes.

The values of the numerical constants in equation (13) may also be extracted directly from the experimental data for each specific material. This of course introduces small variations from the original values used by Williams *et al.* [2]. Knauss [1] has obtained the following values for polyurea ($T_g \approx 223\,\mathrm{K}$):

$$a(T) = 10^{A(T-T_{ref})/(B+(T-T_{ref}))}, \tag{14}$$

$$A = -10, \tag{15}$$

$$B = 107.54\,\mathrm{K}, \tag{16}$$

$$T_{ref} = T_g + 50\,\mathrm{K} = 273\,\mathrm{K}. \tag{17}$$

In the above results, the relaxation-time constants are measured isothermally at various temperatures, and the resulting relaxation curves are shifted accordingly and collected in one single master curve. Thus, the assumed linear hereditary relation, defined by equations (1) and (2), is actually a reasonably good approximation for polyurea. In this manner, the short-time relaxation of the material at higher temperatures is predicted using its relaxation data obtained at low temperatures. This master curve can be fitted using various explicit functional forms. A good power-law form for the shear relaxation modulus is

$$G(t,T) = \frac{T}{T_{ref}}\left(G_\infty + \Delta G\left(\frac{t}{a(T)}\right)^{-\theta_c}\right), \tag{18}$$

$$G_\infty = 22.24\,\mathrm{MPa}, \tag{19}$$

$$\Delta G = 8.42\,\mathrm{MPa}, \tag{20}$$

$$\theta_c = 0.146. \tag{21}$$

However, this compact form has two basic shortcomings that make it unsuitable for explicit numerical calculations. Firstly, it has a singularity at the origin. Secondly, to calculate the stress for a general strain-rate history, the hereditary integral must be evaluated for each instant separately. To remedy this, one may construct a reasonably good representation using a series of simple exponentials, i.e. a discrete set of internal state variables that represent the material's internal relaxation times. Depending on the specific problem, one can then select the number of the relaxation times for a specific time interval to fit the experimental data and thereby to calculate the values of the relaxation times and the coefficient of the associated exponential,

i.e. two material constants for each internal state variable. The general form of such a representation is then

$$G_{ref}(t) = G_\infty \left(1 + \sum_{i=1}^{n} p_i e^{-t/q_i} \right). \tag{22}$$

This description applies directly to the isothermal deformations. When the temperature changes during a deformation (e.g. because of dissipation), we introduce a new time scale,

$$\xi(t) = \int_0^t \frac{d\tau}{a(T(\tau))}, \tag{23}$$

to replace the reduced time, $t/a(T)$, in the expression for the isothermal deformation. In equation (23), the integral is evaluated between 0 and t, to ensure that $\xi = 0$ at no deformation, when $t = 0$ (see Schapery [19]). The linear hereditary integral for the deviatoric part of the deformation is now replaced by

$$\boldsymbol{\sigma}'(t) = \int_0^t 2G(t,\tau)\mathbf{D}'(\tau)d\tau, \tag{24}$$

where

$$G(t,\tau) = \frac{T'}{T_{ref}} G_{ref}(\xi(t) - \xi(\tau)). \tag{25}$$

Note that a new temperature, T', is introduced here, which, as pointed out by Pipkin [17] involves a certain ambiguity, since there is no non-isothermal experimental evidence to suggest how T' should be evaluated. In the present work, we have chosen to set

$$T' = T(\tau), \tag{26}$$

since this choice leads to stable numerical calculations. In what follows, the temperature history is incorporated in the deformation history by replacing $\mathbf{D}'(t)$ with $\mathbf{D}'(t)\, T(t)/T_{ref}$.

At high strain rates, the deformation is essentially locally adiabatic. When the only available heat source is that from the dissipated mechanical energy and the conductive and convective heat losses are slow relative to the strain rates, then the local temperature can be calculated using

$$\frac{\partial T}{\partial t} = \frac{1}{C_V} \frac{\partial W_d}{\partial t}, \tag{27}$$

where C_V is the heat capacity at constant volume (per unit original volume), and W_d is the dissipated work per unit original volume.

In a cyclic loading, the dissipated work can be calculated for a complete cycle of deformation. The instantaneous rate of dissipation will of course depend on the specific model used to represent the material. Care is needed to ensure that the second law of thermodynamics is not violated by allowing the transformation of heat into stored elastic energy. Here, we follow Fung [20] and represent the full response of the material at constant temperature by $n+6$ coupled first-order differential

equations relating n thermodynamic internal state variables and 6 strain components to their conjugate thermodynamic forces and the conjugate stress components. The n hidden internal variables are then eliminated from the differential equations, using linear force-flux relations. The resulting stress–strain relations have the hereditary integral form. With n internal variables, we retrieve equation (22).

The significance of this approach is that the stored energy can be easily calculated at each instant. Therefore, the amount of dissipated energy over a given time interval can be calculated without ambiguity. The rate of energy dissipation associated with the i^{th} internal variable then is

$$\frac{\partial W_d^i}{\partial t} = \frac{1}{\eta^i}(F^i)^2, \tag{28}$$

where η^i and F^i are, respectively, the viscosity and the force associated with the ith internal variable. Using this expression, equation (22) now gives

$$\frac{\partial W_d}{\partial t} = 2G_\infty \frac{T(t)}{T_{ref}} \sum_{i=1}^{n} \frac{p_i}{q_i} \boldsymbol{\varepsilon}_d^i(t) : \boldsymbol{\varepsilon}_d^i(t), \tag{29}$$

where we have set

$$\boldsymbol{\varepsilon}_d^i(t) = \int_0^t e^{-(\xi(t)-\xi(\tau))/q_i} \mathbf{D}'(\tau) d\tau. \tag{30}$$

We must emphasize here that this formula is based on a discrete set of internal variables with linear force-flux relations, as discussed by Fung and others [20–24]. For every relaxation function (22), one can conceive a structure of springs and dashpots that will have this response. Fung [20] shows that all such functions can be arrived at using a spring paralleled with n dashpot-springs put serially. This structure is not unique. For example, the properties of a spring put serially with n paralleled dashpot-springs can be adjusted such that it has the same relaxation function. For these two cases one can show by directly calculating the dissipated energy that equation (29) is the final result when the p's and q's are calculated accordingly. This is not surprising as the strains associated with viscous energy dissipation in equation (30) are attributed to the normal modes of the deformation resulting from the linear force–flux relations and not to the specific representation of springs and dashpots. In short, equation (29) relies only on equation (22) and the linearity assumptions and it does not depend on specific representation of springs and dashpots model.

It is of theoretical interest to note here again that equation (22) is a special function with a discrete set of relaxation times. For a general relaxation function (continuous spectrum) one can show that the dissipated power in equation (29) can be written as

$$\frac{\partial W_d}{\partial t} = \int_{-\infty}^{t} \int_{-\infty}^{t} -2G'(2t - \tau_1 - \tau_2)\dot{\varepsilon}(\tau_1)\dot{\varepsilon}(\tau_2) d\tau_2 d\tau_1. \tag{31}$$

3. Pressure effects

Experimental and theoretical considerations suggest that the viscoelastic properties of polymers are pressure dependent. For the cases considered in the present paper, this is a significant effect. The well-established explanation for this phenomenon is found in works of Ferry [25], Knauss and Emri [26, 27] and Losi and Knauss [28]. It is based on the free-volume content of a polymer: the less available free volume the harder it becomes for the chains to move. Therefore, one can associate the lower free volume due to the high pressure to greater constraint of the thermally activated chain motion. In other words, the higher pressure makes the response of a rubbery polymer closer to that at the glass transition temperature. To incorporate this in our model, we may simply reduce the ambient temperature of the polymer by a quantity proportional to the pressure, i.e. we may set

$$a(T,P) = \frac{\tau(T,P)}{\tau_{ref}} = a(T - C_{tp}P), \tag{32}$$

where P is the pressure and C_{tp} is a time-pressure coefficient that must be established experimentally. In other words, the characteristic relaxation time and the time-shift associated with it are modified again through the reduced temperature. This is, however, a simple approach and must be modified to give appropriate results if a wide range of pressures occurs during a deformation history.

4. Split-Hopkinson bar experiments

We have performed a series of split-Hopkinson bar experiments on polyurea under various conditions. For the general setup and implementation of these tests, see Nemat-Nasser *et al.* [29]. To verify the model discussed in the previous section, a selected set of these experiments is presented here. The complete experimental work performed for characterization of polyurea at various conditions will be published elsewhere. The tests presented here were all performed at an effective engineering strain rate of $3000 \pm 400\,\mathrm{s}^{-1}$. The summary of the experimental parameters is given in table 1.

All 4 tests are performed using a 12.7 mm (half inch) split-Hopkinson bar (maraging steel bars). The sample diameter in the unconfined test is substantially

Table 1. Values of experimental parameters.

Name	Confinement	Diameter (mm)	Length (mm)	Effective strain rate (s^{-1})	Temperature (K)
UC	No	6.17	1.78	3400	294
CL	Yes	12.7	5.08	2600	273
CR	Yes	12.7	5.08	2800	294
CH	Yes	12.7	5.08	2800	333

smaller than that of the bars to accommodate the large radial deformations that occur during the test. For the confined tests, the sample is fitted inside a cylindrical tube of 17.8 mm outside diameter and 26 mm length, machined from VascoMax® C-350 maraging steel. The strains in the transmitted bar can be as low as 10^{-4} (unconfined test). Using a Nicolet MultiPro Digitizer Model 140 with a full range of scale of 15 mV, these signals are recorded without difficulty. For all the tests, a ramped incident pulse is used which allows dynamic equilibrium to be established early in the test. The signals are recorded at every 0.2 μs. In the confined tests, the Cauchy stress and the nominal stress recorded directly are equal. But since the diameter of the sample changes during the unconfined tests, the Cauchy stress must then be estimated. Since under the low pressures observed in the unconfined tests, polyurea is nearly incompressible, we calculated the diameter and the Cauchy stress assuming isochoric deformation. The resulting loading stress–strain curves are shown in figures 1 and 2.

Upon unloading, the dynamics of the test changes from being loaded by a pressure pulse in the incident bar to the soft polyurea releasing the applied stress. Therefore, the time scale of the unloading portion is significantly different from that of the loading portion and the elastic pulses that reflect off the far ends of the Hopkinson bars reach the strain gauges and thus interfere with the measurement of the unloading signals. From the initial part of the unloading curves one observes that, for confined tests, the unloading follows essentially the same stress–strain curve as that of the loading. However, for the unconfined tests, the stress is released much faster than the accumulated strain. This strain is not permanent though and,

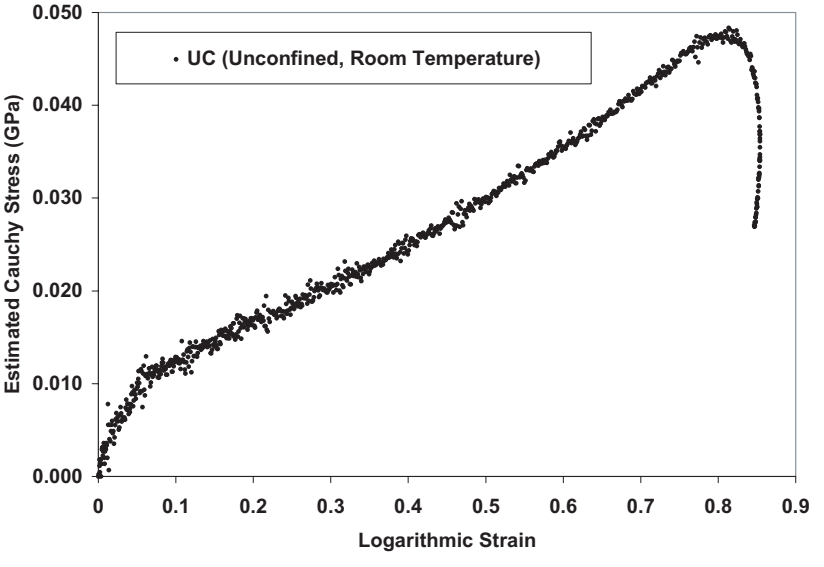

Figure 1. The Cauchy stress–logarithmic strain curve for unconfined polyurea at room temperature, calculated from the nominal stress assuming incompressibility.

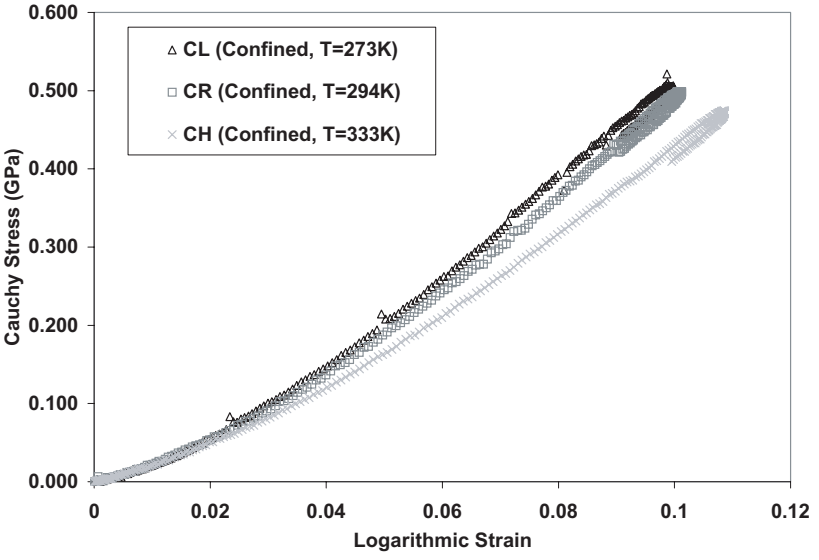

Figure 2. The stress–strain data obtained from confined polyurea Hopkinson bar experiments at indicated temperatures.

in all cases, the sample regained its initial length after the test was completed. Another characteristic of the stress–strain curves in the confined tests is a rather soft initial segment. In these tests, this segment is limited to 1% to 2% strain and occurs at a low rate. In some preliminary tests, this segment was longer and more pronounced. We believe that this is partially due to the fact that the confinement is not perfect at the start of the experiment where there may be some clearance between the sample and the bars. For the experiments discussed here, we manually preloaded the samples slightly, resulting in the disappearance of a major part of the soft segment. However, we believe that the remaining effect is due to a combination of this incomplete contact between the sample and the bars and possibly the material response.

5. Model results and comparison with experimental data

The results of our Hopkinson experiments appear to be in general qualitative agreement with the predictions of the model discussed in the previous sections. To verify this, we have developed a numerical subroutine that incorporates all of the components of the model, and is written to be compatible with the explicit finite-element code, LS-DYNA, which is widely used in research and industry for various applications such as automotive crash-safety design [30]. Some of the quantities that are not usually used in normal structural applications, such as temperature and the reduced time, equation (23), are calculated explicitly and stored. Moreover, the strains associated with viscous flow, equation (30), are also calculated

and stored at each step for all terms in the Prony series, equation (22). The significance of this representation in numerical calculations is now evident. If a general relaxation expression is used, the entire integral in equation (30) will have to be evaluated at each time step. However, the exponential forms in equation (22) make it possible to calculate the increment of the creep strains

$$\boldsymbol{\varepsilon}_c^i(t) = \int_0^t (1 - e^{-(\xi(t)-\xi(\tau))/q_i})\mathbf{D}'(\tau)d\tau = \boldsymbol{\varepsilon}'(t) - \boldsymbol{\varepsilon}_d^i(t), \tag{33}$$

recursively using the current step loading and the information that is stored from the last step [12, 31–33]:

$$\Delta\boldsymbol{\varepsilon}_c^i(t,\Delta t) = (1 - e^{-\Delta\xi/q_i})(\boldsymbol{\varepsilon}'(t) - \boldsymbol{\varepsilon}_c^i(t)) + \left(1 - \frac{q_i}{\Delta\xi}(1 - e^{-\Delta\xi/q_i})\right)\mathbf{D}'(t)\Delta t. \tag{34}$$

The derivation of the stress tensor and the correct form of the dissipated power, equation (29), using the inelastic strains is straightforward now:

$$\boldsymbol{\sigma}'(t) = 2G_\infty\left(\boldsymbol{\varepsilon}'(t) + \sum_{i=1}^{n} p_i\boldsymbol{\varepsilon}_d^i(t)\right). \tag{35}$$

As explained before, the temperature history is stored together with the strain rate history based on equation (26). The simplification resulting from the finite spectrum and the ability to incrementally calculate various parameters at each instant, based on the deformation at the current step and the stored values of the variables, are crucial in most real applications.

The values of the model parameters, i.e. A, B, T_{ref} and G_∞, as given by equations (15)–(17) and (19), and CTE, the coefficient of thermal expansion, are listed in table 2. These values, as well as the values of the dissipation time scales, q's, and their relative stiffnesses, p's, are all based on the results reported by Knauss [1], where, here we have used a least-square fit to the experimental data within a limited range of interest with $n = 4$. The heat capacity at constant volume per unit of original volume, C_V, is measured directly. This value is also verified using an accurate DSC test result (see Amirkhizi [13]). The bulk stiffness parameters, $\kappa(T_0)$ and m, are based on the results of the three confined tests, discussed earlier in this paper. Finally the value of C_{tp}, equation (32), is also estimated from the pressure–shear experimental results presented in the next section.

The final results are shown in figures 3–6. Further mechanical measurements (using a dynamic mechanical analyzer and confined Hopkinson bar tests with

Table 2. Values of constitutive parameters used in the numerical model.

T_{ref} (K)	A	B (K)	C_{tp} (K GPa^{-1})	C_V (J mm^{-3} K^{-1})	CTE (K^{-1})	m (Gpa K^{-1})	n	k_{ref} (GPa)	G_∞ (GPa)
273	−10	107.54	7.2	1.977×10^{-3}	2×10^{-4}	−0.015	4	4.948	0.0224

p_1	p_2	p_3	p_4	q_1 (ms)	q_2 (ms)	q_3 (ms)	q_4 (ms)
0.8458	1.686	3.594	4.342	463.4	0.06407	1.163×10^{-4}	7.321×10^{-7}

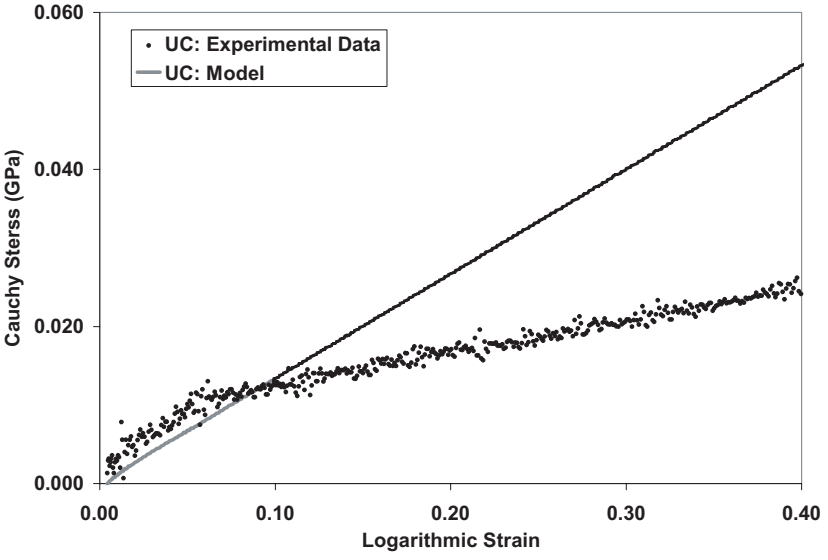

Figure 3. The unconfined polyurea Hopkinson bar test results obtained at $T = 273\,\mathrm{K}$, and the constitutive model result. The instantaneous stiffness of the material reduces at around 8% which is not considered in the model. The Cauchy stress is estimated based on the lateral expansion predicted by the model.

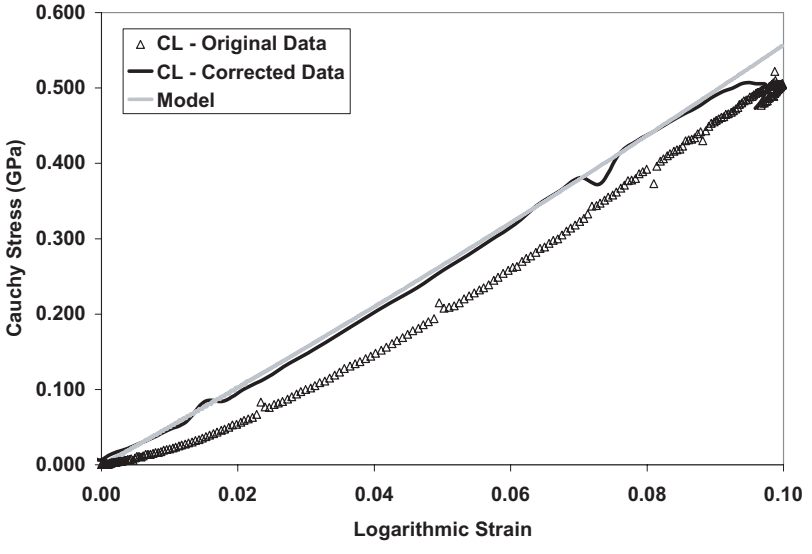

Figure 4. The confined polyurea Hopkinson bar test data obtained at $T = 273\,\mathrm{K}$, and the constitutive model results. The corrected data (CL) curve is obtained by slightly time-shifting and re-centring.

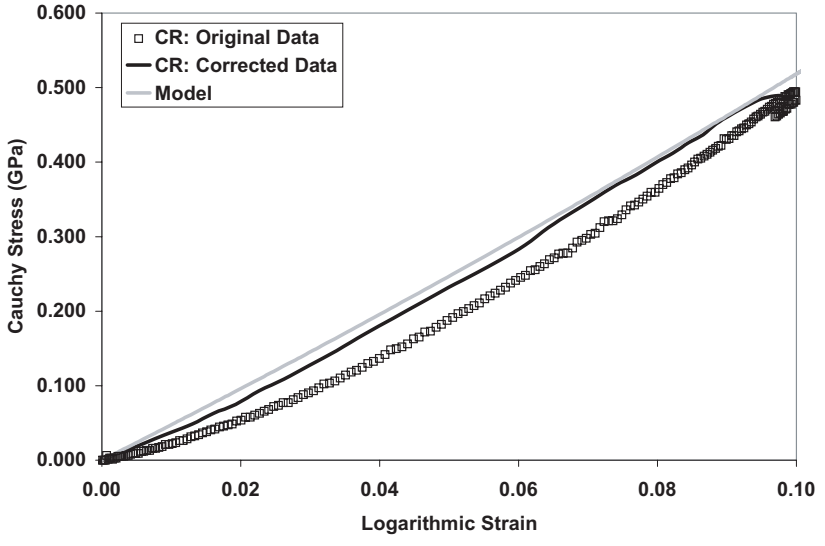

Figure 5. The confined polyurea Hopkinson bar test data obtained at $T = 294\,\mathrm{K}$, and the constitutive model results. The corrected data (CL) curve is obtained by slightly time-shifting and re-centring.

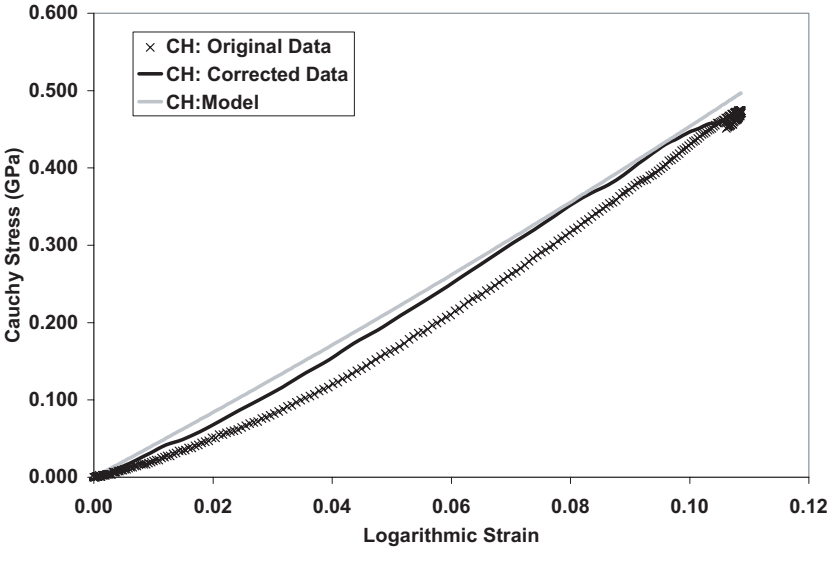

Figure 6. The confined polyurea Hopkinson bar test data obtained at $T = 333\,\mathrm{K}$, and the constitutive model results. The corrected data (CL) curve is obtained by slightly time-shifting and re-centring.

measured hoop strain of the confining cylinder) give values close to those in table 2 (see Amirkhizi [13]). For the unconfined test the model closely predicts the initial slope of the stress–strain curve before the onset of a reduced instantaneous stiffness at about 8% strain. The model does not account for this reduced-stiffness behaviour, generally observed in the unconfined uniaxial response of elastomers. One may approach this shortcoming by using a more elaborate elastic component such as the 8-chain network model of Arruda and Boyce [16]. Note that the effect of the soft initial segment of the confined experiments is more pronounced here. If we remove this segment and assume that the loading starts when full confinement is established, then the modelled results agree closely with the corrected experimental results. We do not intend to find the best fitting parameters here. Rather, we propose that the model discussed in the previous section can reproduce the main qualitative attributes of various independent test results.

6. Application: FEM model of a pressure–shear experiment

The model discussed in previous sections has been used to simulate a pressure–shear test performed at Brown University and documented by Jiao *et al.* [3]. The associated data are given in table 3.

A steel flyer plate impacts at a velocity V_0 a sandwich structure that consists of a front steel plate, a thin layer of elastomer and a rear steel plate. All of the plates are aligned at a constant given angle θ with respect to the velocity direction (see figure 7). Upon impact, two elastic waves are created that travel normally to the surface of the impact at two different velocities. These are: a longitudinal compression wave (high velocity) and a shear wave (low velocity). The impact parameters are set such that the steel plates remain elastic. The longitudinal pressure wave reaches the elastomer layer first and loads it to a maximum stress after a few reverberations. The late arrival of the shear wave to this pre-strained layer makes it possible to study the shear behaviour of highly-compressed materials. Both normal and transverse particle velocities are measured on the back surface of the rear plate using optical methods (see Clifton [34] for a discussion of pressure–shear plate impact experiments).

The propagation of a finite amplitude elastic shear wave in a uniaxially pre-strained layer of elastomer has been discussed before by Nemat-Nasser and Amirkhizi [35]. The observable particle velocity on the back surface of the rear plate

Table 3. Values of geometrical parameters of the pressure–shear test TJ0404 (Courtesy of R. Clifton, Brown University).

Diameter (mm)	Flyer plate thickness (mm)	Front plate thickness (mm)	Rear plate thickness (mm)	Polyurea thickness (mm)	$V_0\,(\mathrm{m\,s^{-1}})$	$\theta\,(^\circ)$
60	6.991	2.896	7.041	0.11	112.6	18

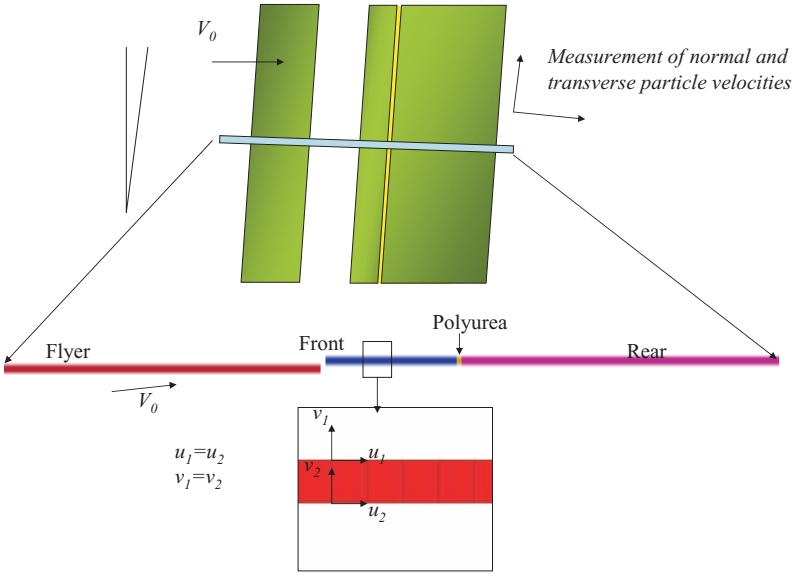

Figure 7. Schematics of the pressure–shear experiment and the FEM model. Top: Flyer plate impacts the front plate at velocity V_0, creating normal and transverse waves that travel and load the polyurea layer and eventually the back plate. Middle: The elements along the centre line passing through the plates and polyurea layer are modelled using LS-DYNA. Bottom: The displacement field of these elements is constrained to produce appropriate lateral confinement while allowing shearing.

consists of stepped rises that finally converge to the impact transverse velocity regardless of the stiffness of the elastomer (see figure 8). Neither of these two properties is observed in the measured transverse velocity by Clifton and Jiao [14]. Instead, there is a single jump at the beginning, followed by a gradual rise in the velocity. The measured value falls considerably short of such predicted final values, as can be seen from data of figure 9.

Full modelling of the pressure–shear test described in table 3 requires a very large number of elements due to the existing high aspect ratios (T:D:D $\sim$ 1:600:600). Even a two-dimensional plane-strain (T:D $\sim$ 1:600) approximation requires far too many elements. However, one can easily retrieve the most relevant information by a quasi-one-dimensional model of the elements along the centre line of the structure (see figure 7). The centre of the whole structure, consisting of the flyer, front, and rear plates and the elastomer layer is modelled with three-dimensional elements using the elastic properties of steel and a nonlinear viscoelastic user-defined constitutive subroutine for polyurea. Boundary conditions are imposed such that the material is confined laterally but allow for shear deformation. However, the free surface boundary condition violates the former, and the fixed surface, contradicts the latter. Therefore, we constrained the top and bottom nodes to have the same displacement degrees of freedom (see figure 7). This maintains a fixed lateral dimension and hence the confining pressure is applied automatically by the finite-element solver.

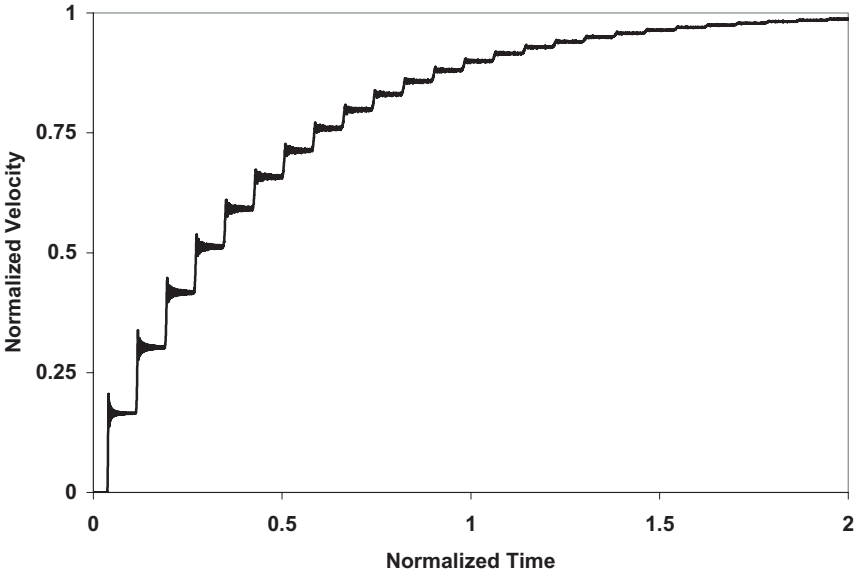

Figure 8. The profile of the normalized transverse particle velocity (divided by $V_0 \sin\theta$) on the back surface of the rear plate for a fully elastic material. The time is normalized through dividing by $(l/(V_0 \sin\theta))$, where l is the thickness of elastomer.

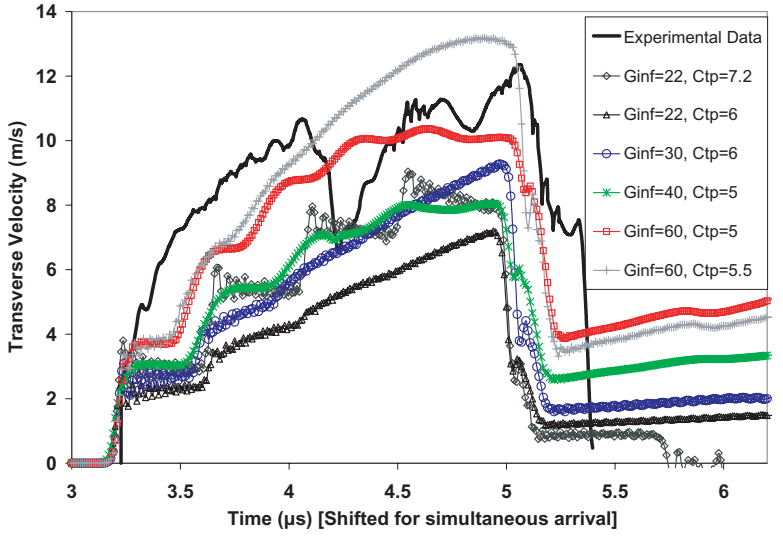

Figure 9. The profile of the transverse particle velocity as measured and calculated on the back surface of the rear plate. The solid curve depicts the experimental results [14] and other curves show the various possible responses by varying two parameters: the equilibrium shear modulus G_∞ (in MPa) and the pressure sensitivity parameter C_{tp} (in K GPa^{-1}).

At the same time, the element can be sheared laterally. This scheme enables us to study the full impact test (until the boundary waves arrive) with a very low number of elements compared to what is required for a full three-dimensional simulation.

The results of the numerical simulations for the transverse particle velocity are shown in figure 9. The bulk properties are modelled as linearly elastic with a constant bulk modulus, $K = 22.5\,\text{GPa}$. The curves in figure 9 depict the rich spectrum of responses that can result under these conditions by varying only two material parameters, the equilibrium shear modulus, G_∞, and the pressure-sensitivity parameter, C_{tp}. The other parameters are the same as those discussed earlier in this paper.

7. Discussion

The calculated normal velocity of the particles at the back face of the rear plate agrees very closely with the experiment up until the unloading (see figure 10). This includes the rise time to the maximum velocity ($\sim$0.6 μs) and the time when the unloading waves arrive ($\sim$2.2 μs). The numerical results predict a full drop of the velocity at the unloading. This is because the unloading waves from both sides, the flyer plate face and the rear plate face, arrive at the same time at the two faces of the elastomer layer. However, the experimental data do not show a complete drop, possibly due to a slight difference in the arrival times of these two release waves.

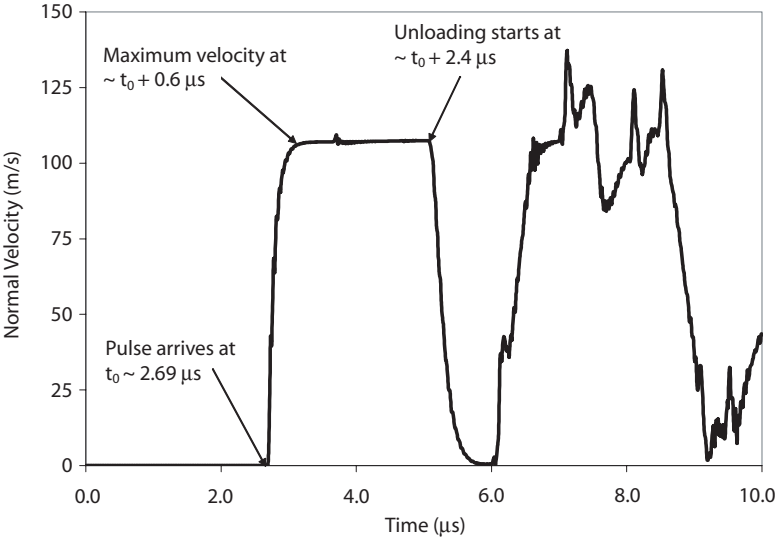

Figure 10. The calculated profile of normal particle velocity. The times shown represent the elapsed time between the arrival of the wave, reaching the maximum velocity/stress, and the arrival of the release wave. The experimental values for these time intervals reported by Jiao *et al*. [3] are, respectively, 0.6 and 2.2 μs which is in good agreement with the numerically calculated values 0.6 and 2.4 μs.

After this unloading, the elastomer undergoes normal tension. The response of polyurea under tension and compression is asymmetric. The numerical model does not incorporate this fact and therefore the results are not valid after the unloading waves have arrived. The timing of the events up to this point is predicted remarkably accurately. If the nonlinearly elastic bulk model discussed before is used in the simulations, the general responses in the normal and shear waves do not change significantly. However, the event timing will not be similar to the experiment, namely the rise time will be much longer than that observed. It must be mentioned here that the significantly higher bulk stiffness observed in this test relative to the Hopkinson data, occurs at about twice the corresponding normal strain, i.e., 21.3% for the pressure-shear test as compared with about 12% for the Hopkinson tests. This amount of volumetric deformation can significantly change the response of the material. It must be noted here that alternative models have been suggested for the elastic bulk response that relate to the results of the lower strain levels, such as the ones observed in Hopkinson bar experiments, to the higher level of volumetric strain that is observed in the pressure–shear test (see, for example, Jiao *et al.* [3]).

The transverse velocity of the particles has complex characteristics. It was previously mentioned that the profile of the measured results does not show step-wise rise except at the beginning of the loading. The flattening of the step-wise profile as observed in the experiment can easily be captured by an appropriate choice of the parameters in the viscoelastic model. This and the fact that the measured transverse velocity rises much more slowly than can be calculated through elasticity considerations are most likely due to the relaxation of the shear stress in the viscoelastic material. The latter phenomenon is readily captured by the viscoelastic model. Finally, the abrupt drop in the measured transverse particle velocity observed at the final stage of the experiment is attributed to the loss of the shear stiffness due to the release of the normal pressure. This release of the normal pressure, and the associated particle velocity, travels at the longitudinal wave speed. However, the resulting effect on the shear stiffness and transverse particle velocity travels at the transverse wave speed. Therefore, this effect is seen later than the arrival of the normal unloading which is observed in the normal velocity measurement. If the measured velocity pulses are shifted back by the time of travel of the normal and shear waves in steel, the unloading of the elastomer and its effect on the shear stiffness will be simultaneous, both in numerical and experimental results. This is confirmed by considering the stresses in the elastomer (see figure 11). This loss of shear stiffness due to the drop in the pressure can be attributed directly to the pressure sensitivity of the viscoelastic relaxation in polyurea; see equation (32).

8. Summary

A complete temperature, pressure and strain-rate dependent nonlinearly viscoelastic constitutive model is developed for the viscoelastic response of polyurea under various conditions. The model parameters are extracted from the experimental results. A Fortran code is developed in order to apply the model to predict the experimental results. This code is compatible for use as a user-defined material

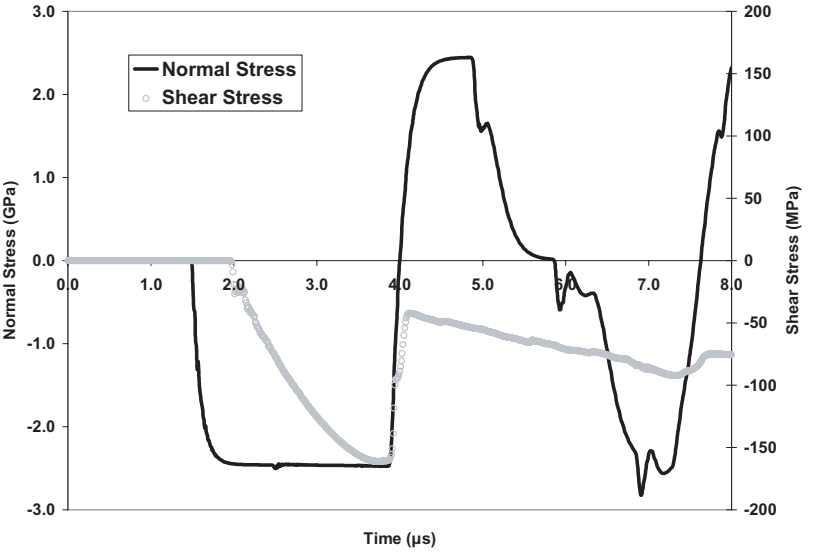

Figure 11. The time history of the normal and shear stress in a typical element in elastomer. The stress scales are different. As the normal stress is released and the elastomer undergoes tension, the shear stiffness immediately drops.

constitutive subroutine with LS-DYNA, a general purpose large-scale finite-element program. Finally, the model is used to reproduce the results of various independent tests, such as confined and unconfined split-Hopkinson bar pressure tests and a pressure–shear test. The predictions of the model are in good agreement with the experimental results under a very wide range of conditions.

Acknowledgements

The authors wish to thank Prof. Rod Clifton and Tong Jiao for sharing with us the data from their pressure–shear experiments and Prof. Wolfgang Knauss for providing us with the relaxation master curve of polyurea. The authors would like to also thank David Owen, Gilbert Lee, Edward Balizer, Willis Mock Jr. and Jeffery Fedderly from the Naval Surface Warfare Center for providing the material and processing techniques along with their experimental results. The authors would like to express their appreciation to Dr. Roshdy Barsoum for many helpful discussions and continued support of their research. This work was supported by ONR N00014-03-M-0172.

References

[1] W.G. Knauss, *Viscoelastic Material Characterization relative to Constitutive and Failure Response of an Elastomer*, Interim Report to the Office of Naval Research (GALCIT, Pasadena, CA, 2003).

[2] M.L. Williams, R.F. Landel and J.D. Ferry, J. Am. Chem. Soc. **77** 3701 (1955).
[3] T. Jiao, R.J. Clifton and S.E. Grunschel, *Shock Compression of Condensed Matter 2005* (American Institute of Physics, New York, 2005).
[4] S.W. Guan, paper presented at the 2nd China International Corrosion Control Conference, Beijing, 4–8 November (2002).
[5] O. Bayer, Angew. Chem. A **59** 257 (1947).
[6] The Dow Chemical Company, *Isonate® 143L; Modified MDI* (Dow Chemical, Midland, MI, 2001).
[7] Air Products Chemicals, Inc., *Polyurethane Specialty Products* (Air Products and Chemicals, Allentown, PA, 2003).
[8] G. Lee, *Unpublished Communication* (NSWC, Carderock, VA, 2004).
[9] W. Mock and E. Balizer, paper presented at Polyurea Properties and Enhancement of Structures under Dynamic Loads, Airlie, VA (2005).
[10] D.R. Bland, *The Theory of Linear Viscoelasticity* (Pergamon Press, Oxford, 1960).
[11] R.M. Christensen, *Theory of Viscoelasticity*, 2nd edn (Academic Press, New York, 1982).
[12] ABAQUS Inc., *ABAQUS/Theory manual, Version 6.5* (ABAQUS Inc. Providence, RI, 2005).
[13] A.V. Amirkhizi, paper presented at the 2005 SEM Annual Conf. and Expo. on Experimental and Applied Mech., Portland, OR, June 7–9 (2005).
[14] R.J. Clifton and T. Jiao, paper presented at ERC ACTD Workshop, Cambridge, MA (2004).
[15] L. Anand, Comput. Mech. **18** 339 (1996).
[16] E.M. Arruda and M.C. Boyce, J. Mech. Phys. Solids **41** 389 (1993).
[17] A.C. Pipkin, *Lectures on Viscoelasticity Theory* (Springer-Verlag, New York, 1972).
[18] R. Rahouadj, J-F. Ganghoffer and C. Cunat, *Mech. Res. Comm.* **30** 119 (2003).
[19] R.A. Schapery, Polym. Engng Sci. **9** 295 (1969).
[20] Y.C. Fung, *Foundations of Solid Mechanics* (Prentice-Hall, Englewood Cliffs, NJ, 1965).
[21] M.A. Biot, J. Appl. Phys. **25** 1385 (1954).
[22] J. Meixner, Z. Naturforsch. A **9** 654 (1954).
[23] B. Coleman and M. Gurtin, J. Chem. Phys. **47** 597 (1967).
[24] R.A. Schapery, in *Proceedings of the IUTAM Symposium on Irreversible Aspects of Continuum Mechanics*, edited by H. Parkus and L.I. Sedov (Springer-Verlag, Berlin, 1968).
[25] J.D. Ferry, *Viscoelastic Properties of Polymers*, 2nd edn (John Wiley & Sons, New York, 1970).
[26] W.G. Knauss and I.J. Emri, Comput. Struct. **13** 123 (1981).
[27] W.G. Knauss and I.J. Emri, Polym. Engng Sci. **27** 86 (1987).
[28] G.U. Losi and W.G. Knauss, Polym. Engng Sci. **32** 542 (1992).
[29] S. Nemat-Nasser, J. Isaacs and J.E. Starrett, Proc. R. Soc. A **435** 371 (1991).
[30] J.O. Hallquist, *LS-DYNA Theoretical Manual* (LSTC, Livermore, CA, 1998).
[31] R.L. Taylor, K.S. Pister and G.L. Goudreau, Int. J. numer. Meth. Engng **2** 45 (1970).
[32] M. Henriksen, Comput. Struct. **18** 133 (1984).
[33] J.C. Simo and T.J.R. Hughes, *Computational Inelasticity* (Springer-Verlag, New York, 1998).
[34] R.J. Clifton, in *Mechanics Today*, edited by S. Nemat-Nasser, Vol. 1 (Pergamon Press, New York, 1974).
[35] S. Nemat-Nasser and A.V. Amirkhizi, Wave Motion **43** 20 (2005).